Mechanical characterization of oxide coating–interconnect interfaces for solid oxide fuel cells

Sajedur R. Akanda [a], Mark E. Walter [a,*], Neil J. Kidner [b], Matthew M. Seabaugh [b]

[a] Department of Mechanical and Aerospace Engineering, The Ohio State University, 201 West 19th Avenue, Scott Laboratory, OH 43210, USA
[b] NexTech Materials Ltd., 404 Enterprise Drive, Lewis Center, OH 43035, USA

ARTICLE INFO

ABSTRACT

This paper reports on the characterization of interfaces between oxide coatings and metallic interconnects that are used in planar solid oxide fuel cells. With the reduction of operating temperatures to 800 °C, it is possible to replace ceramic interconnects with less expensive stainless steels. However, when incorporating chromia-forming metallic interconnects, steps must be taken to inhibit chromium poisoning. One approach to prevent chromium poisoning, is to deposit dense, protective coatings, such as manganese cobalt spinel oxide (MCO). The brittle nature of MCO makes it susceptible to damage under mechanical and thermal stresses during operation. A four point bend experiment is designed to assess the strength and adhesion of reduced and oxidized coatings deposited on SS441 or Crofer interconnects. Resulting tensile cracking patterns on the convex side of bend specimen are used to quantify the interfacial shear strength with a shear lag model. Using energy based fracture mechanics, interfacial fracture energy is calculated from the strain at the onset of coating spallation. Scanning electron microscopy images of the cracked coating surfaces are processed to analyze the failure mechanisms, crack spacing and spalled areas. At 3% strain, the weakest interface is found in the Crofer system with the oxidized coating.

© 2012 Elsevier B.V. All rights reserved.

1. Introduction

It is well known that for fuel cells to reach practical power levels, individual cells must be repeated to form a fuel cell stack. Interconnects are the components that separate individual cells and provide the means to complete the electrical circuit. Thus interconnects maintain the uniform fuel and air flow as well as play a critical role in efficiency and power density of fuel cell stacks. Since opposite sides of interconnects are exposed to reducing (fuel) and oxidizing (air) environments, the resulting chemical potential gradients place severe constraints on selecting the most appropriate material. Additional design requirements for an interconnect are as follows: excellent electrical conductivity, chemical and physical inertness in high temperature corrosive environments, compatible coefficients of thermal expansion with the anodes and cathodes of a stack, good thermal conductivity, high strength and creep resistance, and low material and fabrication costs [1]. In light of these requirements, chromia forming ferritic stainless steels such as Allegheny Ludlum (AL) 441-HP or Crofer 22 APU are the most promising materials for interconnects in solid oxide fuel cells.

A significant drawback to chromia-forming interconnects is chromium degradation or chromium poisoning. Depending on the atmosphere at the cathode, chromium rich alloys form chromium trioxides CrO_3, or chromium hydroxides $CrO_2(OH)_2$. Upon combining with oxygen ions in the cathode active area, the chromium compounds reduce back to chromia scale, Cr_2O_3. Thus the chromia scale formation results in decreased cathode active area. In addition, the electrically insulating nature of chromia scales increases the contact area specific resistance (ASR) between the interconnect and cathode. As a consequence, the performance and efficiency is significantly degraded [2].

It is therefore critical to inhibit chromium migration from interconnects to cathodes. One way to achieve the necessary chemical inertness of interconnects is to perform surface modification by applying a thin, dense protective coating on the surface of interconnects. The protective layer acts as a diffusion barrier to the chemical reaction between the interconnects and the corrosive environment, thus slowing the rates of chromium oxide scale formation and inhibiting chromium volatility in the cathode active area.

Researchers have recently applied manganese cobalt spinel oxide (MCO) as a protective layer on the cathode side of interconnects in an SOFC stack. Larring and Norby [3] observed increased capability of MCO to prevent chromium evaporation compared to that of a pervoskite coating. In addition, with iron-doping of the spinel MCO, it is possible to achieve excellent electrical conductivity. Yang et al. [4] studied thermally grown MCO with a nominal composition of $Mn_{1.5}Co_{1.5}O_4$ on Crofer22 APU substrates. The substrate was slurry coated and then heat treated in reducing
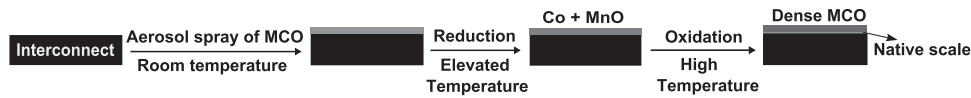
Fig. 1. Steps for processing MCO coatings on interconnects.

and oxidizing environments. Their experimental results indicate decreased ASR between LSF cathodes and the interconnects due to significant inhibition of scale growth. The spinel coating acted as an effective barrier to both inward oxide ion diffusion and outward chromium migration.

The ceramic MCO is extremely brittle. The mechanical integrity of this protective oxide layer is affected by complex thermo-chemical–mechanical conditions. The protective oxide layer which prevents the chemical attack can be severely damaged by thermal and mechanical stresses generated during oxide scale growth, thermal cycling and mechanical loading during fuel cell operation [5]. The resulting thermo-mechanical stresses can result in coating fracture and failure. The coating–substrate interface plays an important role in the mechanisms of coating failure and spallation. For weaker coating–substrate interfaces, an oxide scale would first buckle under high compressive stresses and then spall when through-thickness cracks develop [6]. For relatively strong interfaces, shear cracks form in the coating, which causes shear sliding in the cracked segment and finally spallation in the protective coating [6]. For SOFCs, when the protective coating layer fails or loses adhesion with interconnects, uncoated interconnect metal is exposed to the high temperature corrosive environment. The resulting damage and degradation to the interconnect can cause a significant drop in the electrochemical performance of the SOFC. Therefore, it is necessary to characterize the coating–interconnect interfaces and develop a scientific understanding of the mechanical response of protective interconnect coatings. Understanding the decohesion mechanisms in the coating–interconnect interface and failure mechanisms in the coating will have a positive impact on reliability assessment of interconnects in high temperature applications.Liu et al. [7] at Pacific Northwest National Laboratory have incorporated indentation techniques to characterize coating–interconnect interfaces in SOFCs. Together with finite element simulations, they performed stair stepping indentation tests to quantify the interfacial shear strength of coating–oxide scale–Crofer tri-layer systems in SOFCs. The critical load at which coating spallation occurred was used to quantify the interfacial shear strength. However, indentation creates a plastically deformed zone beneath the surface which limits the depth of indentation to be less than coating thickness [8]. Therefore the indentation method is difficult to apply to coatings that are only a few microns thick. It is also important to note that the nanoindentation technique samples a very small volume of the interface and would not capture the stochastic nature of the interface.

In the present work, room temperature four point bend experiments are performed to investigate the coating–interconnect interfaces. The experimental set up is designed in such a way as to place the brittle coating under tensile stresses. The spacing between the resulting saturated parallel tensile cracks on the coating surface is incorporated in a shear lag model to quantify the interfacial shear strength. At higher strains, spallation of the coating occurs. The strain at the onset of spallation is used to calculate the interfacial fracture energy.

2. Experimental

2.1. Materials

Interconnects coated with spinel MCO are manufactured at NexTech Materials Ltd. NexTech's processing steps are shown in Fig. 1.

In the first step, an MCO suspension is applied through an aerosol spray deposition process onto an interconnect at room temperature. The suspension is prepared with MCO powder with a nominal composition of $Mn_{1.5}Co_{1.5}O_4$ by using an appropriate binder. The thickness of the coating ranges from 10 to 15 μm. The specimen is then heat treated in a controlled reduction. The reduction heat treatment reduces the MCO coating into two distinct components: metallic Co and MnO. The organic binder is burned out during the firing. In the final step, the specimen is exposed to a high temperature oxidation heat treatment in air. The oxidation heat treatment is an essential step for obtaining a dense MCO coating. During the oxidation heat treatment, selective oxidation of the alloying elements in the substrate forms a very thin layer (3–5 μm) of native oxide scale between the MCO coating and the interconnect. The dual phase native scale is mainly composed of $(Mn,Cr)_3O_4$ on the top with a chromia rich sub-layer at the bottom. SEM images of reduced and oxidized MCO coatings are shown in Fig. 2(a) and (b), respectively.
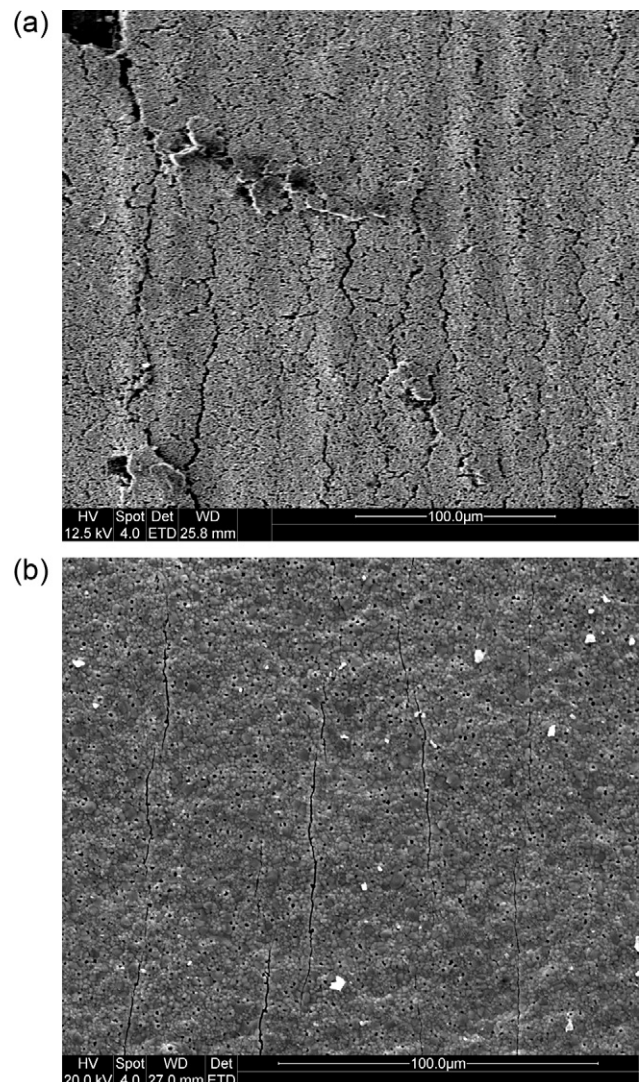

Fig. 2. SEM images of (a) reduced MCO–SS441 and (b) oxidized MCO–Crofer.
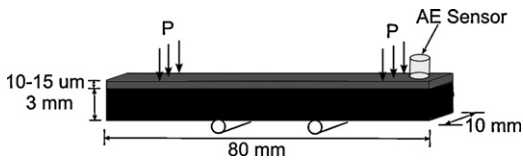
Fig. 3. Experimental setup to characterize the coating–interconnect interface.

In the present work, two types of ferritic stainless steel interconnect substrates are considered: AL 441-HP (SS441) and Crofer 22 APU. SS441 is composed mainly of 17.6% Cr and 0.33% Mn by weight with minor amount of alloying elements such as Si, Ni, and S and with the balance being Fe. Crofer 22 APU is an Fe–Cr–Mn steel specifically developed for SOFC interconnect applications. It has 22.3% Cr with 0.45% Mn, other alloying elements, and a balance of Fe. The advantage of Crofer 22 over SS441 is that it has enhanced electrical conductivity in the native oxide scale due to the presence of higher amount of Mn [9]. In addition to having higher amounts of Cr and Mn, Crofer has also trace amounts of rare earth elements, for example, 0.06% of La [9].

2.2. Bend experiments

The experiment is set up such that the coating will experience tensile stresses during bending. The loading configuration and dimensions of the test specimen are shown in Fig. 3. The inner and outer loading spans are 20 and 60 mm, respectively. The stresses at the outer surfaces of coating–interconnect test specimen are calculated from the applied loads by the method of Timoshenko [10]. Surface strains are obtained from a conventional strain gage attached to the uncoated side of the test specimen. An acoustic emission (AE) sensor that is couple to a Vallen System AMSY-4 is placed on the coated side of the specimen to monitor scale failure. The AE sensor detects the transient surface waves generated from cracking and other failure and deformation phenomena that release strain energy. After the AE signal is pre-amplified by 34 dB, the signal threshold is set to 40 dB to eliminate unwanted noises from the load frame and test environment. To accurately identify the acoustic emission events associated with coating spallation, the coating was observed in situ with a high magnification camera lens. The stress–strain data and AE data are synchronized for subsequent analysis of failure mechanisms.

3. Theory

3.1. Interfacial shear strength

The tensile loading failure mechanisms in a brittle coating on a ductile substrate are schematically illustrated in Fig. 4(a). When the tensile stresses exceed the critical tensile stress of the coating, initial thru-thickness tensile cracks are produced in the coating. The initial cracks, also called primary cracks, are created by stresses generated from the applied bending moment. After formation of the primary cracks, tensile stresses are no longer transferred to the cracked segment of the coating directly from the bending moment. Instead, the tensile stresses are transferred from the ductile substrate to the coating segments through interfacial shear stresses or what is also called "shear-lag." As a consequence of stress transfer through shear at the interface, tensile stresses continue to develop in the segmented coating layers, creating further thru-thickness tensile cracks. The cracks from shear-lag are known as secondary cracks as they are not generated from the bending moment directly. Crack density increases as the applied strain increases until at some point, the formation of the parallel thru-thickness cracks saturates [11].
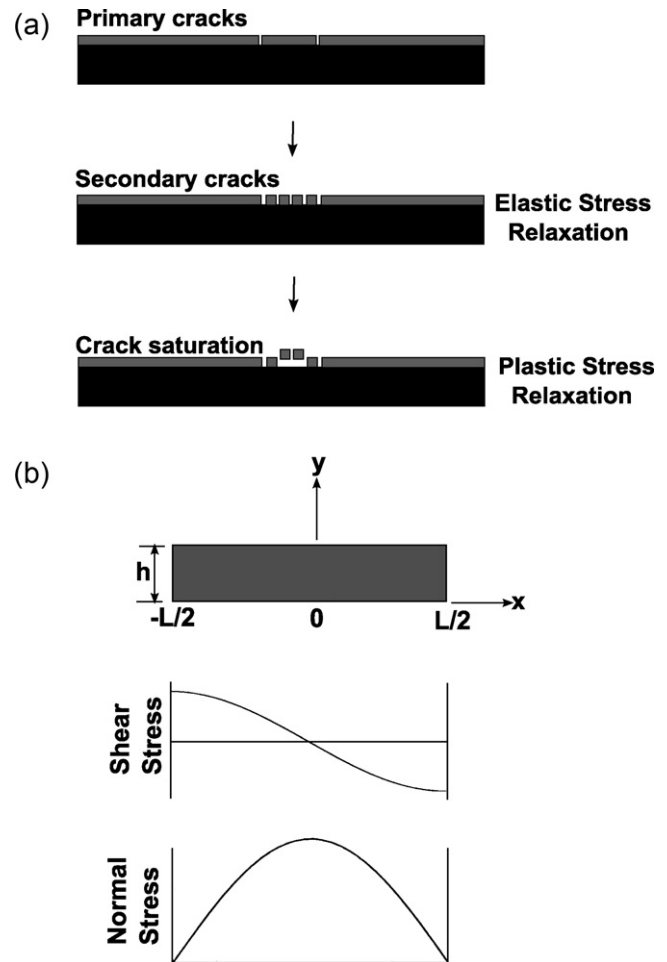

Fig. 4. (a) Schematic of failure mechanisms in brittle coatings during bend experiment. (b) Schematics of shear and normal stress distributions in a coating segment.

The formation of secondary thru-thickness tensile cracks is described as elastic stress relaxation and can be modeled by shear lag theory [12]. For a coating segment of length L and thickness h, Fig. 4(b) shows a shear stress distribution at the interface and the resulting normal stress distribution in the coating. Although bending creates a thru-thickness stress gradient, the coating is 0.5% of the substrate thickness and the effects of the stress gradient thru the coating thickness are therefore negligible. At both ends of the cracked surfaces of the segment, all the stresses are supported by the substrate resulting in maximum shear and minimum normal stress at both ends of the segment. The shear stress is lowest at the midpoint of the interface and the tensile stress is highest at the middle of the coating segment. When the maximum tensile stress exceeds the critical stress of the coating, a new cracked segment is formed. The maximum shear stress (τ_{max}) at the interface can be related to the critical tensile stress of the coating (σ_{ct}), through coating thickness (h), and crack spacing (L) by the following equation:

$$\tau_{max} = kh\frac{\sigma_{ct}}{L} \tag{1}$$

where k is an integration constant which depends on the assumed shear stress distribution [13]. If the interface is considered to be purely elastic with linear shear stress distribution along the interface, k takes the value of 4 [14]. For an ideal plastic interface where the shear stress distribution is assumed to be constant, k is 2 [14]. In the present case, a sinusoidal shear stress is considered along the interface to allow the interface to have limited

plastic stress relaxation next to the thru-thickness cracks. In this case, k is π which is between ideal elastic and plastic behavior [13].

Once the shear strength of the interface has been exceeded, the shear stresses are relaxed by non-elastic mechanisms such as interface slip next to the tensile cracks or by substrate yielding at the base of the thru-thickness cracks. This phase is described as plastic stress relaxation, and secondary crack formation saturates during this phase [13]. Interface slip is followed by interface delamination. By measuring the saturated crack spacing, it is possible to calculate the interfacial shear strength from Eq. (1).

3.2. Interfacial fracture energy

At higher strains, coating spallation is observed. If it is assumed that the coating is perfectly adhered to interconnect and only elastically strained during the experiment, elastic strain energy will be stored in the coating. At some point, it is energetically favorable to release the stored elastic energy as interfacial fracture, resulting in coating spallation. The interfacial fracture energy, G can be calculated from the relation [15].

$$G = Wh$$

where W is the stored elastic energy density in the coating and h is the coating thickness. W is a function of in-plane stress–strain evolution in the coating along both the longitudinal and transverse axes. Despite the bend loading, stress perpendicular to the interface would be very small and are thus assumed to be neglected [13]. During the experiment, the coating deforms elastically whereas the metal interconnect undergoes elastic and plastic deformation. For a continuous, un-cracked coating, the tensile stresses developed in the coating during elastic interconnect deformation; can be expressed as a function of applied tensile strain on the coating by the following equation [15]:

$$\sigma_c^x = \frac{E_c}{(1 - \nu_c^2)}(1 - \nu_s \nu_c)\varepsilon_c^x$$

where E is Young's Modulus, ν is Poisson ratio, ε is strain and σ is stress. The subscript 'c' stands for MCO coating and the subscript 's' stands for substrate. The superscript 'x' corresponds to the longitudinal axis. If the interconnect undergoes plastic deformation, the tensile stress–strain relation in the coating takes the following form [15]:

$$\sigma_c^x = \frac{E_c}{(1 - \nu_c^2)}\left[\varepsilon_c^x + \nu_c\left(\frac{1}{(1 + \varepsilon_c^x)^{1/2}} - 1\right)\right]$$

During elastic deformation of the interconnect, the compressive stresses generated in the coating along the in-plane transverse axis can be calculated by [15]

$$\sigma_c^z = \frac{E_c}{(1 - \nu_c^2)}(\nu_c - \nu_s)\varepsilon_c^z$$

here the superscript 'z' corresponds to the in-plane transverse axis. During plastic deformation of the interconnect, compressive stresses can be described by the following relation [15]:

$$\sigma_c^z = \frac{E_c}{(1 - \nu_c^2)}\left[\varepsilon_c^z + \nu_c\left(\frac{1}{(1 + \varepsilon_c^z)^2} - 1\right)\right]$$

As mentioned in Section 2.2, the longitudinal compressive strains of the surface of the substrate on the uncoated side of the test specimen are obtained from a strain gage. From four point bend theory and for a very thin coating ($h_c \ll h_s$), the tensile strains in the un-cracked coating are equal in value to the compressive strains from the strain gage and the compressive strains in the coating

along the in-plane transverse axis are equal to the in-plane transverse compressive strains of the substrate. Considering the area under the stress–strain curve of the MCO coating, the stored elastic energy in the coating at the onset strain of spallation (ε_{sp}) can be calculated from the following relation [15]

$$W = \int_0^{\varepsilon_{sp}} \sigma d\varepsilon$$

If the first thru-thickness transverse crack and the onset of spallation occur at nearly the same strain, both the tensile and compressive stress evolution would need to be considered. However, if the coating spallation occurs at a comparatively higher strain, the tensile stresses are relaxed by the formation of the cracked segments in coating, and only the compressive stresses are involved in computing the fracture energy [15].

4. Results

4.1. Cumulative AE

The flexural stress–strain curve of a coating–interconnect specimen together with cumulative AE data is presented in Fig. 5. Two types of interconnects, SS441 and Crofer^{TM}, were considered. For each type of interconnect, the effects of both the reduction and oxidation heat treatment were investigated. Both SS441 and Crofer are ferritic stainless steels, and the young's modulus ($\sim$200 GPa) and yield stress ($\sim$350 MPa) were found to be same for both the substrates. Since the coating is extremely thin, it has no effect on the stress–strain curve. The stress–strain curve shown in Fig. 5 is representative of all coating–substrate systems.
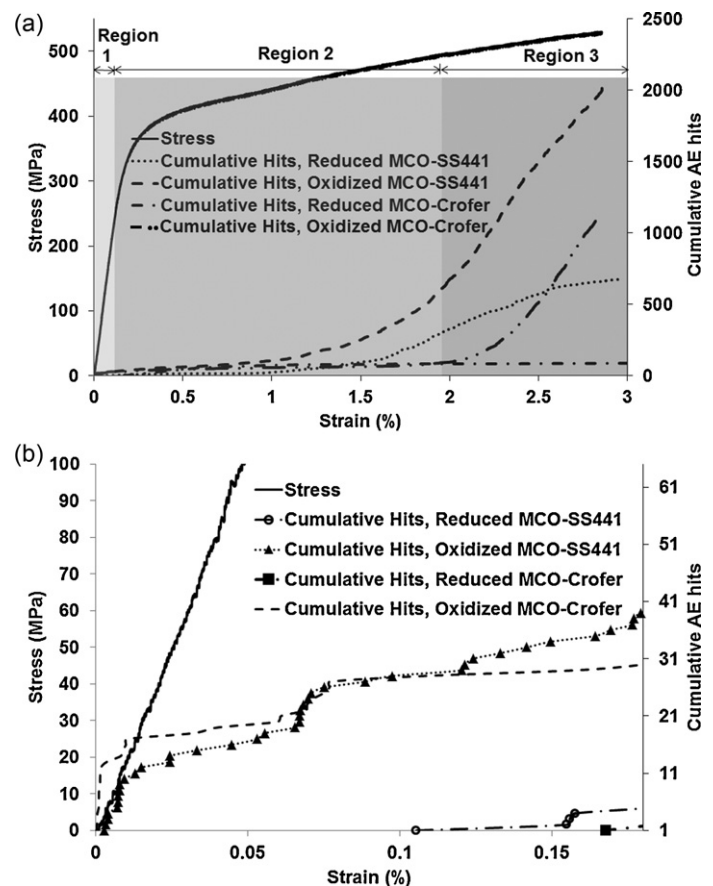

Fig. 5. (a) Experimental stress–strain curve synchronized with cumulative AE data. (b) An enlarged view of Region 1 of cumulative AE data.

Table 1
Average critical tensile stress (σ_{ct}), interfacial shear strength (τ), interfacial fracture energy (G_c), and % spall area for each type of test specimen.

Interconnect	Average σ_{ct} (MPa)		Average τ (MPa)		Average G_c (J m^{-2})		% Spall area at 3% strain	
	Reduced	Oxidized	Reduced	Oxidized	Reduced	Oxidized	Reduced	Oxidized
SS441	131.76	3.70	130.32	3.70	4.94	2.76	3.23	9.43
Crofer^{TM}	225.50	1.38	229.95	2.0	–	10.02	No spall	18.80

The AE data provides information on cracking events. The cumulative AE curve for each type of test specimen was plotted by adding the individual AE hits cumulatively. In Fig. 5(a) the cumulative AE curve reveals three distinct regions of AE activity. In the initial region which is shown in an enlarged view in Fig. 5(b), the cumulative AE hits are observed to increase with strain in the range of approximately 0–0.2% strain. This region represents the formation of thru-thickness tensile cracks in the coating during elastic stress relaxation. The first AE hit is considered to take place at the critical strain for the tensile crack formation in the coating. Assuming elastic deformation of the coating, the critical tensile stress of the coating is calculated from the critical strain and mechanical properties of the coating. The mechanical properties of MCO coating are taken to be $E = 124.7$ GPa and $\nu = 0.36$ [7].

For each type of test specimen, ten experiments were conducted. The critical tensile stresses obtained from all the experiments were found to be consistent in each type of test specimen. The average value of critical tensile stresses for each type of test specimen is tabulated in Table 1. As is observed in Fig. 5(b) and Table 1, the oxidation heat treatment decreases the critical stress of the coating significantly. The more dense structure of oxidized MCO is favorable for cracks generated from a pre-existing defects or voids. The higher slopes of the cumulative AE curves for oxidized test specimen indicate that the oxidized MCO has higher crack density than that of the reduced MCO.

After the elastic stress relaxation, the saturation of formation of tensile cracks during plastic stress relaxation is illustrated by a relatively flat Region 2 in the cumulative AE curves shown in Fig. 5(a). Presumably because of the 40 dB threshold setting, the plastic stress relaxation is not detected by the AE sensor. Due to the statistically variable nature of the interface strength, there may still be some thru-thickness crack formation in Region 2. In other words, one section of the interface may still have sufficient strength to transfer shear stresses to the coating whereas the shear stresses of the interface in other sections are no longer sufficient to cause damage in the coating.

Finally in the third region, a sharp increase in slope of the cumulative AE curves is observed at higher strains for each type of test specimen except the reduced MCO–Crofer. The strain at which the slope begins to increase sharply is the critical strain for spallation of the coating. The critical strain for spallation was also identified in situ coating observation by a high magnification camera lens. Post-experiment SEM observations found no spallation for the reduced coated Crofer interconnects, which is consistent with the lack of AE events in Region 3 for this specimen.

4.2. Interfacial shear strength

After the bend experiments, SEM images of the coating were taken. Fig. 6 shows images of saturated parallel transverse cracks of MCO coating on SS441 and Crofer interconnect. The tensile stresses were applied perpendicular to the in-plane transverse cracks. Crack spacing was measured with Matlab image processing tools. Coating thickness was measured from the back scattered SEM images of the cross-section of the tested specimen. After incorporating the values of saturated crack spacing and thickness into Eq. (1), interfacial shear strength was calculated for each type of test specimen. The calculated values of interfacial shear strength are plotted
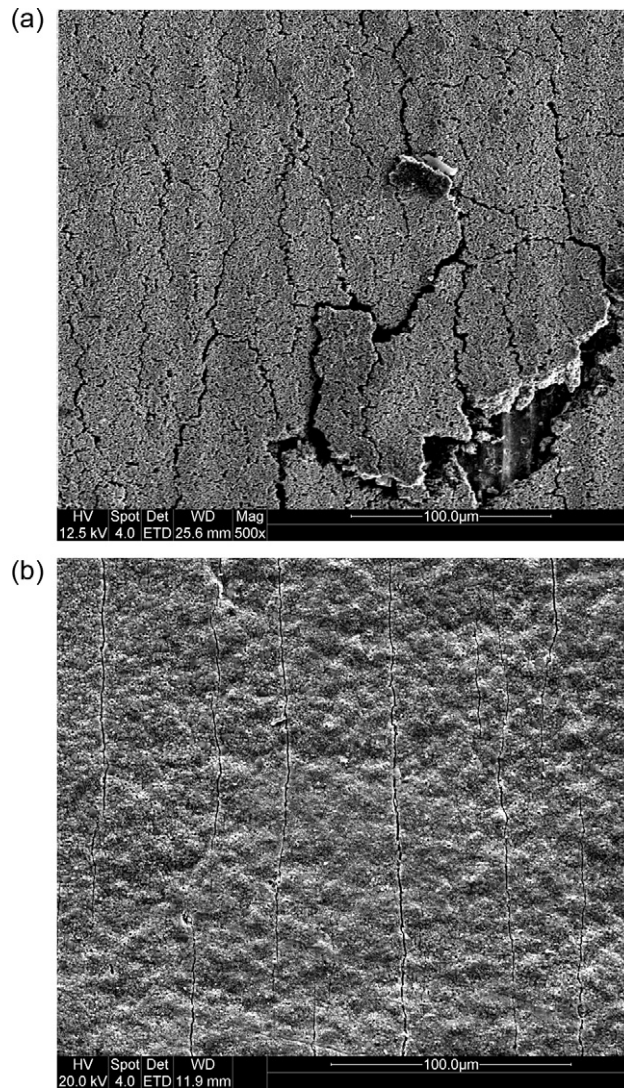
(a)

(b)

Fig. 6. Saturated parallel in-plane transverse cracks in (a) reduced MCO on SS441. (b) Oxidized MCO on Crofer.

in Fig. 7. As a result of interface defects as well as variability in bulk microstructure, interfacial shear strength is going to be statistical in nature. There are a number of stochastic variables in Eq. (1) that would provide statistical variability. For example, the coating strength varies from point to point, the thickness is not constant, and crack spacing varies throughout. Since crack spacing incorporates other physical phenomena, it was decided to plot interfacial shear strength for all the different crack spacing measurements. The mean shear strength was calculated from at least 50 measurements and is provided in Table 1. Liu et al. [7] found much higher interfacial shear strengths for a coating–oxide scale–Crofer system. It is not possible to compare the present results with those of Liu et al. because differences in processing temperatures would have a significant effect on the interface strength.
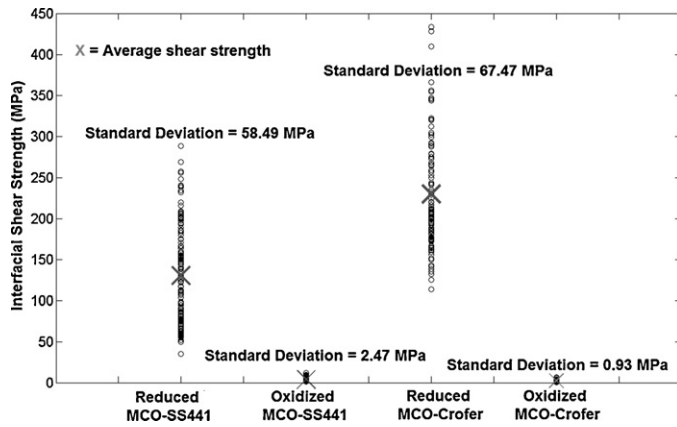
Fig. 7. Calculated values of interfacial shear strength for each type of test specimen.

It is observed in Fig. 7 that the interfacial shear strength has higher statistical variability for reduced test specimen. Comparing Fig. 6(a) and (b) it is found that the oxidized MCO has more continuous in-plane transverse cracks with more uniform crack spacing than reduced MCO. Furthermore, in Fig. 7 the interface is clearly weaker after oxidation heat treatment for both types of interconnects.

4.3. Interfacial fracture energy

The critical strain of spallation obtained from the acoustic emission data and the in situ observations with high magnification camera lens is utilized to calculate the interfacial fracture energy for each type of test specimen by the method described in Section 3.2. Table 1 gives the values of interfacial fracture energy. The interfacial fracture is preceded by buckling of coating due to Poisson induced compressive stresses [16]. The bucking is assumed to initiate from a pre-existing defect at the interface. The pre-existing defect may originate from the interface slip induced delamination during plastic stress relaxation. With increase of the applied strain, thru-thickness cracks develop at the location of the buckled coating where the combination of stresses and defects in the coating exceed the fracture toughness of the coating and finally spallation occurs. Fig. 8 shows an example of the early coating buckling with thru-thickness cracks developed in the coating. The SEM images of the cracked and spalled surfaces obtained at 3%
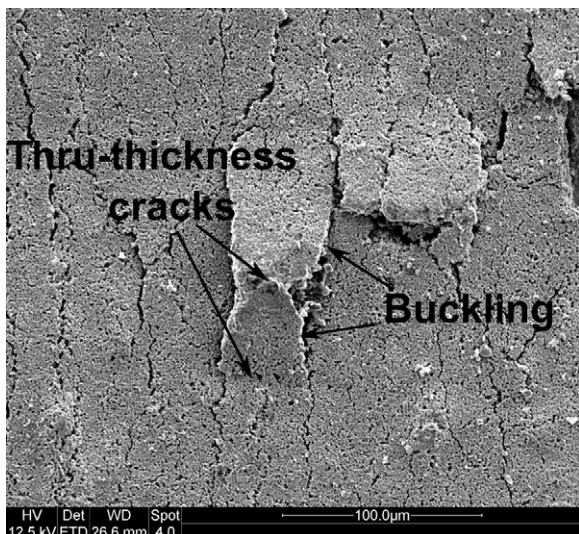

Fig. 8. Buckling of MCO coating before spallation (reduced MCO–SS441 at 3% strain).

strain were processed in Matlab image processing tools to measure the percentage spallation area (%SA). In Fig. 9, the SEM images and their corresponding processed images are presented for each type of test specimen. In the processed images, the white portions denote the spalled areas whereas the black portions indicate the un-spalled coatings. The values of %SA are also tabulated in Table 1. As illustrated in Fig. 9, reduced MCO–Crofer specimens have almost no spallation. The little-to-no spallation in reduced MCO–Crofer is also consistent with the AE results in Fig. 5(a) where there is no increase in slope in Region 3 observed for reduced MCO–Crofer. The tensile yield strength of the Crofer substrate is approximately 350 MPa [17]. The shear yield strength is therefore 200 MPa and 175 MPa from the Von Mises criteria and the Tresca criteria, respectively. In Table 1, the average interfacial shear strength for reduced MCO–Crofer has been found to be 230 MPa. Since the interfacial shear strength exceeds the shear yield strength for the reduced MCO–Crofer specimen, it is likely that yielding of substrate relaxes the interfacial shear stresses. The absence of interface slip induced delamination inhibits the buckling of the coating. This results in almost no spallation of reduced MCO on Crofer within 3% strain. Since critical strain for spallation in the reduced MCO–Crofer specimens was not measureable during the experiment, the interfacial fracture energy was not calculated for this specimen type. Although it has higher interfacial fracture energy than oxidized and reduced MCO-SS44, oxidized MCO–Crofer has the maximum %SA at 3% strain. The sizes of the spalled sections are also comparatively larger. Therefore, the fracture energy distribution of oxidized MCO–Crofer interface is such that, after attaining the critical energy for fracture at approximately 2% strain, extensive coating spallation takes place with a small increase of applied strain. Oxidized coating has the lowest adhesion with Crofer interconnect at 3% strain.

5. Discussion

5.1. Effect of reduction and oxidation heat treatments

As is listed in Table 1, oxidation heat treatment decreases the tensile strength of the MCO coating and both the interfacial shear strength and interfacial fracture energy. The oxidation heat treatment yields a denser but more brittle MCO which is favorable for thru-thickness crack propagation. Energy dispersive spectroscopy (EDS) was performed on the spalled areas. The EDS results are presented in Fig. 10. For reduction heat treatments, the spallation occurs at the interface between the interconnect and the MCO coating. Conversely, for oxidation heat treatments, porous, chromium rich native oxide scale is found in the spalled sections. Therefore, for oxidized specimens the fracture is observed to occur along the brittle interface between the native oxide scale and the MCO coating instead of the native oxide scale–interconnect interface. The interfacial shear strength and the interfacial fracture energy in Table 1 for oxidized specimen refer to the interface between the native oxide scale and the MCO coating. The native oxide scale–MCO coating interface is a much weaker interface than the ductile–brittle interface between the interconnect and the native oxide scale. In their research using nanoindentation on a coating–oxide–Crofer tri-layer system, Liu et al. [7] also report that interfacial fracture occurs along the native scale–coating interface.

5.2. Effect of interconnect composition

When only the reduction heat treatment is considered, Crofer™ has better bonding with MCO coatings than SS441. The rare earth (RE) element present in Crofer substrate (lanthanum) improves the adhesion between coatings and interconnects [9].
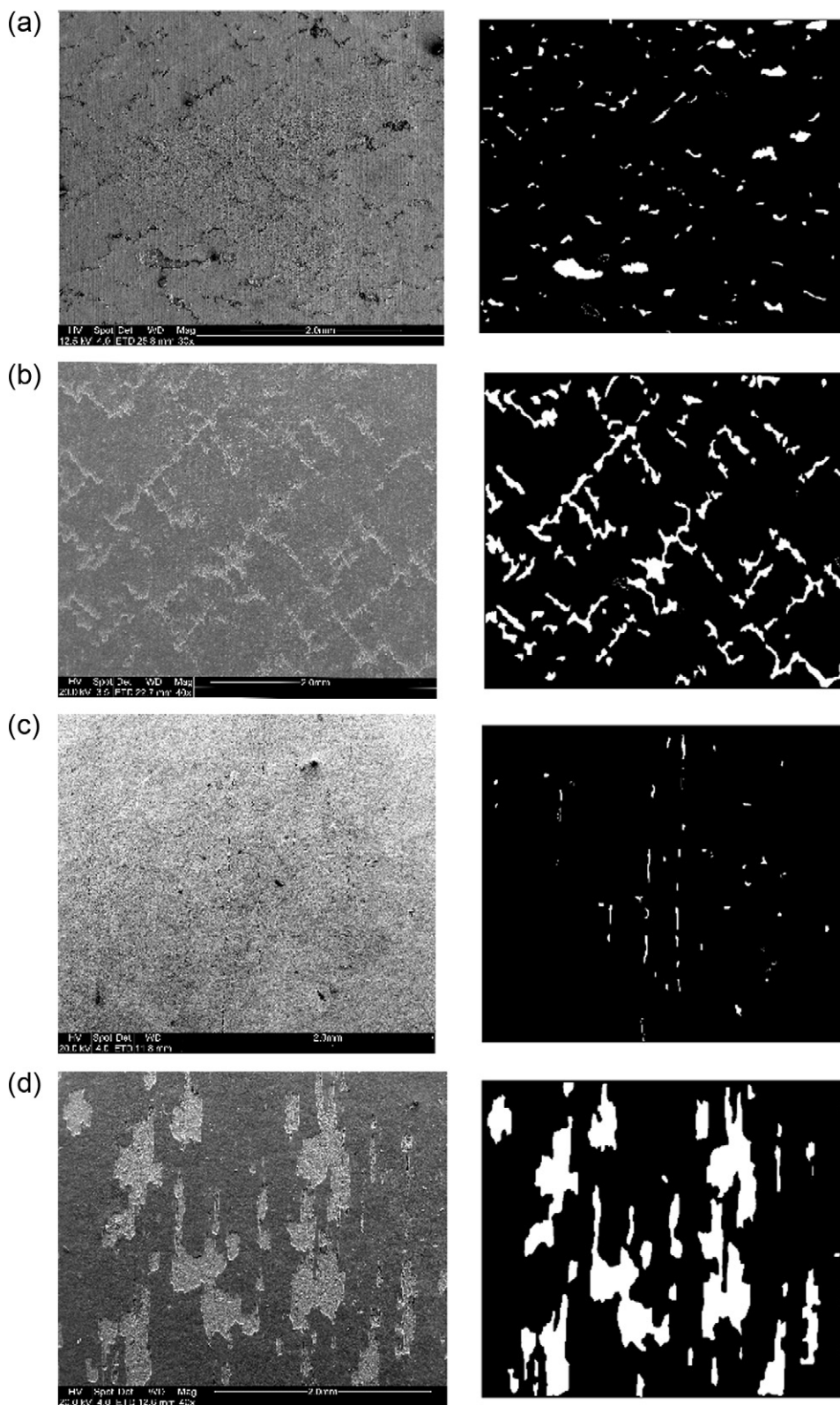
Fig. 9. Representative SEM and processed images of MCO coating surfaces at 3% strain (a) Reduced MCO–SS441. (b) Oxidized MCO–SS441. (c) Reduced MCO–Crofer. (d) Oxidized MCO–Crofer.

Conversely, after oxidation heat treatments, the tensile strength of the coating and the shear strength of the interface become lower for Crofer interconnects than for SS441. It is interesting to observe in Table 1 that although the interfacial shear strength is lower for oxidized MCO–Crofer than that of oxidized MCO–SS441, the

fracture energy of interface is higher for oxidized MCO–Crofer. Therefore, it can be concluded that the interfacial shear strength does not correlate directly with the adhesion of coating; rather shear strength indicates the capability of stress transfer from the substrate to the coating. Shear stresses exceeding the shear
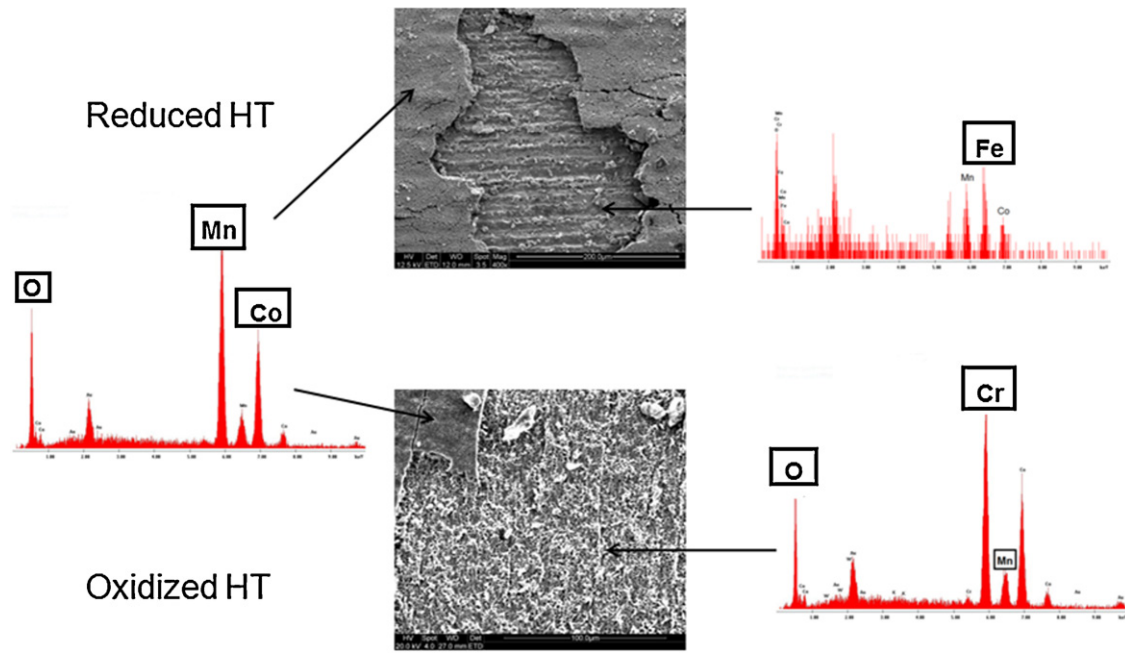
Fig. 10. SEM and EDS analysis of spalled sections of reduced coating on SS441 and oxidized coating on Crofer.

strength of the interface do not necessarily cause instant coating spallation. This can be seen in Fig. 5(a) where the Region 2 in the cumulative AE curves separates the crack saturation due to shear strength in Region 1 from spallation due to interface fracture in Region 3. At 3% strain, the significant amount of spallation for oxidized MCO–Crofer specimen reveals that the adhesion quality between oxidized MCO coating and Crofer interconnects degrades at high strain.

6. Conclusions

Four point bend experiments were performed to characterize the interfaces between MCO coatings and SS441 or Crofer interconnects. The shear strength and fracture energy at the interfaces were determined. Effects of both the reduction and oxidation heat treatments were investigated. Interfacial shear strength calculated by a shear lag model, measures the capability of the interface to transfer stresses from interconnect to the coating. Interfacial fracture energy is more related to the assessment of adhesion of the coating. Oxidation heat treatment is a necessary step to perform in processing MCO coatings in order to inhibit chromium poisoning of interconnects by producing a denser protective coatings on interconnects. However, oxidation heat treatment reduces the tensile strength of MCO coating by making the coating more brittle. In addition, the brittle chromium rich native oxide scale formed by oxidation degrades the interface and lower the adhesion of MCO coating. The weakest interface is found to be between the MCO coating and the native oxide scale. Furthermore, in case of oxidation heat treatment, the interfacial fracture energy is higher for Crofer interconnect than that of SS441 but at 3% strain Crofer has the maximum amount of coating spallation.

The formation of native oxide scales on metallic interconnects is inevitable in high temperature fuel cell applications. With increasing operation time, the thickness of the native oxide scale will increase and this thicker native oxide scale is expected to result in degradation of the adhesion strength of the interconnect coating. As a consequence, in addition to loosing the protective properties of the coating, it is also expected that the thicker native oxide scale

and damaged interface will result in lower electrical conductivity, thus decreasing the power density of the SOFC stack.

The next step in the study of protective interconnect coatings is to develop the ability to predict the lifetime of the coating under operating conditions. Stresses at the interface would be highest during thermal cycling and could be determined from analytical models that incorporate the different thermal expansion coefficients. By performing the four point bend experiments described in this paper on test specimens oxidized for different periods of time, the evolution of interfacial shear strength and fracture energy with operating time can be characterized. Lifetime prediction would then be based on comparison of the evolving interface properties with the stresses present during thermal cycling.

References

[1] W.Z. Zhu, S.C. Deevi, Material Science and Engineering 348 (2003) 227–243.
[2] J. Puranen, J. Lagerbom, L. Hyvarenan, M. Kylmalathi, O. Himanen, M. Pihlatie, J. Kiviaho, P. Vuoristo, Journal of Thermal Spray and Technology 20 (2010) 154–159.
[3] Y. Larring, T. Norby, J. Electrochem. Soc. 47 (2000) 3251–3256.
[4] Z. Yang, G. Xia, S.P. Simner, J.W. Stevenson, J. Electrochem. Soc. 152 (2005) 1896–1901.
[5] B. Borie, C.J. Sparks, J.V. Cathcart, Acta Matallurgica 10 (1962) 691–695.
[6] H.E. Evans, Material Science and Engineering 120 (1989) 139–146.
[7] W.N. Liu, X. Sun, E. Stephen, M.A. Khaleel, Journal of Power Sources 189 (2009) 1044–1050.
[8] P.Y. Hou, A. Atkinson, Materials at High Temperatures 12 (1994) 119–125.
[9] S.P. Simner, M.D. Anderson, G.G. Xia, Z. Yang, L.R. Pederson, J.W. Stevenson, Journal of Electrochemical Society 152 (2005) A740–A745.
[10] S. Timoshenko, Strength of Materials, Part 1, D. Van Nostrand Company Inc., New York, 1930.
[11] M. Yanaka, Y. Tsukahara, N. Nakaso, N. Takeda, Journal of Material Science 33 (1998) 2111–2119.

[12] M.M. Nagl, S.R.J. Saunders, W.T. Evans, D.J. Hall, Corrosion Science 35 (1993) 965–977.
[13] M.M. Nagl, W.T. Evans, D.J. Hall, S.R.J. Saunders, Oxidation of Metals 42 (1994) 431–449.
[14] A. Strawbridge, H.E. Evans, Engineering Failure Analysis 2 (1995) 85–103.
[15] S.C. Ambhorn, F.R. Dherby, F. Toscan, Y. Wouters, A. Galerie, M. Dupeux, Material Science and Technology 23 (2007) 497–501.
[16] A.G. Evans, J.W. Hutchinson, Int. J. Solid Structures 20 (1984) 455–466.
[17] Crofer 22 APU Material Data Sheet, No. 4046, June 2008 Edition.